

# Large-eddy simulation of turbulent flow and dispersion over a complex urban street canyon

Kiyoung Moon · Jeong-Min Hwang · Byung-Gu Kim ·  
Changhoon Lee · Jung-il Choi

Received: 29 July 2013 / Accepted: 24 December 2013 / Published online: 24 January 2014  
© Springer Science+Business Media Dordrecht 2014

**Abstract** Turbulent flow and dispersion characteristics over a complex urban street canyon are investigated by large-eddy simulation using a modified version of the Fire Dynamics Simulator. Two kinds of subgrid scale (SGS) models, the constant coefficient Smagorinsky model and the Vreman model, are assessed. Turbulent statistics, particularly turbulent stresses and wake patterns, are compared between the two SGS models for three different wind directions. We found that while the role of the SGS model is small on average, the local or instantaneous contribution to total stress near the surface or edge of the buildings is not negligible. By yielding a smaller eddy viscosity near solid surfaces, the Vreman model appears to be more appropriate for the simulation of a flow in a complex urban street canyon. Depending on wind direction, wind fields, turbulence statistics, and dispersion patterns show very different characteristics. Particularly, tall buildings near the street canyon predominantly generate turbulence, leading to homogenization of the mean flow inside the street canyon. Furthermore, the release position of pollutants sensitively determines subsequent dispersion characteristics.

**Keywords** Large-eddy simulation · Urban street canyon · Pollutant dispersion · Tall building · Subgrid scale model · Turbulent flow

## 1 Introduction

Understanding the turbulent flow and pollutant dispersion mechanism in an urban area is becoming more important from the perspective of air quality control, urban climate change,

---

K. Moon · J. Choi (✉) · C. Lee  
Department of Computational Science and Engineering, Yonsei University,  
50 Yonsei-ro, Seodaemun-gu, Seoul 120-749, Republic of Korea  
e-mail: jic@yonsei.ac.kr

J.-M. Hwang · B.-G. Kim · C. Lee  
Department of Mechanical Engineering, Yonsei University,  
50 Yonsei-ro, Seodaemun-gu, Seoul 120-749, Republic of Korea

civil planning and wind engineering. Over the last decade, many studies concerning dispersion and climate in urban areas have been performed [1–6]. To predict pollutant dispersion accurately, the wind field information inside an urban canopy should be precisely described. In many air pollution models, however, the parametrization of an urban area as a surface roughness has typically been adopted [7–9]. These models consider buildings of an urban site as roughness elements of the terrain in the average sense. On the neighborhood scale (1 or 2 km) according to the classification in Britter et al. [10], buildings may still be treated statistically. While this approach has an advantage of fast calculation, detailed elements, such as urban street canyons, cannot be properly specified. A street canyon is a key element affecting wind and dispersion in a megacity such as Seoul since tall buildings are typically aligned along the edges and significantly disturb high-altitude wind fields.

Many experimental studies have been conducted for modeling of flow and pollutant dispersion in street canyon by means of field experiments for a real urban area [11, 12], cubical obstacles [13], laboratory-scale wind tunnel experiments for a simplified street canyon [14–16], and scaled real urban sites [17, 18]. During the past two decades, many numerical studies have also been conducted using various types of numerical simulation with Computational Fluid Dynamics (CFD) for modeling of flows and dispersions in a street canyon, see Li et al. [19]. Reynolds-averaged Navier–Stokes (RANS) models have been widely used in street-canyon flow research on the effects of geometric configurations of buildings as well as atmospheric boundary layer conditions [19–27]. Many previous studies have indicated that RANS models have a difficulty in precise predictions of the separation region behind a bluff body and are deficient in calculating near-field pollutant dispersion concentrations around buildings [28–31]. On the other hand, large-eddy simulations (LES) have been utilized in order to more accurately predict flow and pollutant dispersion near simple obstacle arrays [29, 32–38]. However, most numerical studies focused on flow over simple geometries, such as a group of uniformly arranged cubes, different height cubes with the same square base, or a two-dimensional street canyon. Even direct numerical simulation was adopted to calculate flow over urban-like cubical obstacles, although it is limited to low Reynolds numbers [39].

Recently, several researchers [28, 30, 31, 40–42] have adopted LES models with a massively parallel computation to predict flow field and pollutant dispersion over an urban street canyon. Hanna et al. [40] showed that LES and RANS models produce similar wind flow patterns, as well as good agreement with winds observed during a field experiments in New York City. Patnaik et al. [41] used the monotone integrated LES methodology for urban dispersion in New York City and Los Angeles. Liu et al. [42] used LES models with a domain decomposition method which treats surrounding buildings as roughness elements for prediction of wind field and pollutant dispersion from vehicle exhaust in the Rua Do Campo area of Macau. Tominaga and Stathopoulos [30] performed a comparative study between LES (based on Smagorinsky model) and RANS models for pollutant dispersion in a street canyon and found that the LES model can provide a better prediction of the horizontal diffusion of pollutant concentration. Also, Gousseau et al. [28] performed pollutant dispersion simulations in an actual urban environment focused on near-field dispersion using LES (based on dynamic Smagorinsky model) and RANS models. They confirmed that LES model shows a better performance without requiring any parameter input to solve the dispersion equation.

The objective of the present study is to investigate flow and pollutant dispersion characteristics over a complex urban street canyon with various wind directions. A particular emphasis is placed on the effect of tall buildings on the pedestrian-level wind environment and pollutant dispersion patterns. To this end, we utilize a LES technique combined with Geographic Information System (GIS) database containing actual rendering of urban street canyons. Additionally, the effect of LES subgrid scale (SGS) models on flow field have been

systematically investigated, but it is yet unclear whether the local influence of SGS models is important in real urban scale flow. We also perform assessments of SGS models such as the conventional Smagorinsky model [43] and recently proposed Vreman model [44] through an investigation of the contribution of the SGS stress to the total stress and eddy viscosity distribution.

This paper is organized as follows: Sect. 2 contains the model descriptions, validation and numerical methods. Two kinds of SGS models of LES are assessed in Sect. 3. In Sects. 4 and 5, wind fields, turbulent statistics, and dispersion patterns are examined in detail for three different wind directions. Conclusions follow in Sect. 6.

## 2 Numerical approach

The numerical model used in our simulations is a modified version of the Fire Dynamics Simulator (FDS)[45]. For this study, a new SGS model and several integral routines were implemented into FDS. The original FDS code adopts a second-order predictor-corrector scheme in time and a second-order central difference scheme in space.

### 2.1 LES model

In LES, large-scale three-dimensional unsteady turbulent motions are directly resolved, whereas the effects of the smaller scale motions are modeled into SGS models. It is well known that the dynamic SGS model [46] has a good accuracy for various flow types, particularly near the solid wall. However, the dynamic model is costly in the calculation of eddy viscosity, and it needs at least one homogeneous direction. For these reasons, in this study, two simple SGS turbulence models are tested for the turbulent flow over complex urban streets. One is the constant coefficient Smagorinsky model (hereinafter denoted by SM), and the other is the Vreman model (VR) which is relatively new.

The filtered Navier–Stokes equations, the species transport equation for each gaseous species, the energy conservation equation and the equation of state [45] are written as follows,

$$\frac{\partial \rho}{\partial t} + \frac{\partial \rho \bar{U}_i}{\partial x_i} = 0, \tag{1}$$

$$\frac{\partial \rho \bar{U}_j}{\partial t} + \frac{\partial \rho \bar{U}_i \bar{U}_j}{\partial x_i} = -\frac{\partial \bar{p}}{\partial x_j} - \frac{\partial \tau_{ij}^r}{\partial x_i} + \frac{\partial}{\partial x_i} \left( \rho \nu \frac{\partial \bar{U}_j}{\partial x_i} \right), \tag{2}$$

$$\frac{\partial \rho \bar{Y}_\alpha}{\partial t} + \frac{\partial \rho \bar{Y}_\alpha \bar{U}_i}{\partial x_i} = -\frac{\partial q_{\alpha,i}}{\partial x_i} + \frac{\partial}{\partial x_i} \left( \rho D_\alpha \frac{\partial \bar{Y}_\alpha}{\partial x_i} \right) + \dot{m}_\alpha, \tag{3}$$

$$\frac{\partial \rho \bar{h}_s}{\partial t} + \frac{\partial \rho \bar{h}_s \bar{U}_i}{\partial x_i} = \frac{D \bar{p}}{Dt} - \frac{\partial e_i}{\partial x_i} + \frac{\partial}{\partial x_i} \left( k \frac{\partial \bar{T}}{\partial x_i} \right) + \frac{\partial}{\partial x_i} \left( \sum_\alpha \bar{h}_{s,\alpha} \rho D_\alpha \frac{\partial \bar{Y}_\alpha}{\partial x_i} \right), \tag{4}$$

$$\bar{p} = \rho R \bar{T} / W. \tag{5}$$

Here,  $\bar{U}_i$ ,  $\bar{p}$  and  $\bar{T}$  are filtered velocity vector, pressure and temperature, respectively, with an overline denoting a filtering process.  $W$  and  $\rho$  are the molecular weight and the density of air-pollutant mixture and  $\nu$  is the kinematic viscosity of the fluid and  $R$  is the universal gas constant. Note that  $\frac{D \bar{p}}{Dt} = \frac{\partial \bar{p}}{\partial t} + \bar{u} \cdot \nabla \bar{p}$ . The sensible enthalpy ( $\bar{h}_s$ ) is defined as

$$\bar{h}_s = \sum_\alpha \bar{Y}_\alpha \bar{h}_{s,\alpha}, \tag{6}$$

$$\bar{h}_{s,\alpha}(\bar{T}) = \int_{T_0}^{\bar{T}} C_{p,\alpha}(T')dT'. \tag{7}$$

Here,  $\bar{Y}_\alpha$ ,  $D_\alpha$  and  $C_{p,\alpha}$  are mass fraction, the diffusivity and the specific heat capacity of each gaseous pollutant species, respectively, and  $\dot{m}_\alpha$  is the mass source of each gas which models release of a pollutant gas.

The anisotropic residual-stress tensor ( $\tau_{ij}^r$ ) is defined by

$$\tau_{ij}^r = \tau_{ij}^R - \frac{1}{3}\tau_{kk}^R\delta_{ij}, \tag{8}$$

with residual-stress tensor ( $\tau_{ij}^R$ ) denoting

$$\tau_{ij}^R = \rho(\overline{U_i U_j} - \bar{U}_i \bar{U}_j). \tag{9}$$

The residual species flux ( $q_{\alpha,i}$ ) and residual heat flux ( $e_i$ ) are given by

$$q_{\alpha,i} = \rho(\overline{Y_\alpha U_i} - \bar{Y}_\alpha \bar{U}_i), \tag{10}$$

$$e_i = \rho(\overline{h_s U_i} - \bar{h}_s \bar{U}_i). \tag{11}$$

The anisotropic residual-stress tensor, the residual species flux and the residual heat flux can be modeled using the eddy viscosity ( $\nu_T$ ),

$$\tau_{ij}^r = -2\rho\nu_T \bar{S}_{ij}, \tag{12}$$

$$q_{\alpha,i} = -\frac{\rho\nu_T}{Sc_t} \frac{\partial \bar{Y}_\alpha}{\partial x_i}, \tag{13}$$

$$e_i = -\frac{\rho\nu_T}{Pr_t} \frac{\partial \bar{h}_s}{\partial x_i}, \tag{14}$$

where  $Sc_t$ ,  $Pr_t$  and  $\bar{S}_{ij}$  are the turbulent Schmidt number (= 0.5 in this study), turbulent Prandtl number (= 1.0 in this study) and the filtered rate of strain given by

$$\bar{S}_{ij} = \frac{1}{2} \left( \frac{\partial \bar{U}_i}{\partial x_j} + \frac{\partial \bar{U}_j}{\partial x_i} \right), \tag{15}$$

respectively.

For SM, the eddy viscosity is modeled as

$$\nu_T = (C_s \Delta)^2 \bar{S}. \tag{16}$$

Here,  $C_s$  is the Smagorinsky coefficient that is typically in the range of 0.1 ~ 0.2 for most flows.  $C_s = 0.1$  recommended by Shah [47] for flow past a blunt obstacle is adopted in our study. The characteristic filtered rate of strain ( $\bar{S}$ ) is

$$\bar{S} = \sqrt{2(\bar{S}_{ij}\bar{S}_{ij})}. \tag{17}$$

The filter width is given by

$$\Delta = (\Delta x \Delta y \Delta z)^{1/3}, \tag{18}$$

where  $\Delta x$ ,  $\Delta y$  and  $\Delta z$  are the grid size in the  $x$ ,  $y$  and  $z$  directions, respectively. Eddy viscosity for VR takes the following form.

$$\nu_T = C_v \sqrt{\frac{B_\beta}{\bar{\alpha}_{ij}\bar{\alpha}_{ij}}} \tag{19}$$

where

$$\bar{\alpha}_{ij} = \frac{\partial \bar{U}_j}{\partial x_i}, \tag{20}$$

$$B_\beta = \beta_{11}\beta_{22} - \beta_{12}^2 + \beta_{11}\beta_{33} - \beta_{13}^2 + \beta_{22}\beta_{33} - \beta_{23}^2, \tag{21}$$

$$\beta_{ij} = \sum_{m=1}^3 \Delta_m^2 \bar{\alpha}_{mi} \bar{\alpha}_{mj}. \tag{22}$$

Here,  $C_v$  is a model coefficient. In our study,  $C_v$  is set as  $2.5C_s^2$ , which holds under the assumption that  $|\bar{S}_{ij}| = |\bar{\alpha}_{ij}|$ .  $\beta_{ij}$  is positive semi-definite, which means  $B_\beta \geq 0$ . Vreman [44] showed that the second invariant of  $\beta_{ij}$  and the SGS dissipation are zero for 13 cases among 320 possible velocity derivative matrices  $\bar{\alpha}_{ij}$ , whereas SM produces non-zero values for those cases except the trivial one. Note that the density and temperature variations are not considered in the present study.

The wall model based on Werner and Wengle[48] is used for the insufficient grid resolution near the wall as follows:

$$u^+ = z^+ \quad \text{for } z^+ \leq 11.81, \tag{23}$$

$$u^+ = A(z^+)^B \quad \text{for } z^+ > 11.81, \tag{24}$$

where  $u^+$  is the nondimensional streamwise velocity normalized by the friction velocity,  $z^+$  is the nondimensional wall-normal distance in wall-unit,  $A = 8.3$  and  $B = 1/7$ , respectively.

### 2.2 Model Validation

Before applying our numerical model to a real urban street canyon, we validate our model against the wind-tunnel experiment by Castro et al. [49] conducted over a staggered cubical array. Performance of the two SGS models (SM, VR) for two different resolutions are investigated. Domain size is  $4h \times 4h \times 8h$ , in the streamwise, lateral, and vertical directions, respectively, where  $h$  is a cube height. Two uniform grid resolutions,  $40 \times 40 \times 80$  and  $80 \times 80 \times 160$ , are tested. Cubes are located at the bottom and the top of the channel in a mirrored manner instead of using the slip boundary condition at the domain top. Periodic boundary conditions are imposed in the streamwise and lateral directions, and the no-slip condition is imposed at solid walls. A constant pressure gradient that balances the same friction velocity ( $u_*$ ) as the experimental conditions is applied to maintain flow in the streamwise direction. The Reynolds number based on the friction velocity and cube height is 923. All statistics were obtained by time averaging for  $2100T$ , where  $T = h/u_*$ , after time reaches  $3500T$  to ensure temporal convergence.

Figure 1a, b show the streamwise mean velocity ( $U$ ) profiles and the root mean square velocity fluctuation ( $u'$ ) profiles normalized by the friction velocity obtained behind a cube, respectively. In the legend, ‘SM\_10’ refers to the case with 10 grids per side of the cube with SM, and ‘VR\_20’ refers to 20 grids per side of the cube with VR. Figure 1c, d show those measured profiles in front of a cube. Mean velocity profiles and streamwise turbulence show good agreement with the wind-tunnel data. Particularly, mean velocity in the canopy region is well predicted by VR. In the case of streamwise turbulence, the VR prediction is more consistent with the experimental data than that of SM above the canopy height. In the canopy region, in front of or behind the cube, both SGS models fail to correctly predict the level of turbulence. On the other hand, the lateral and vertical turbulence (not shown here)

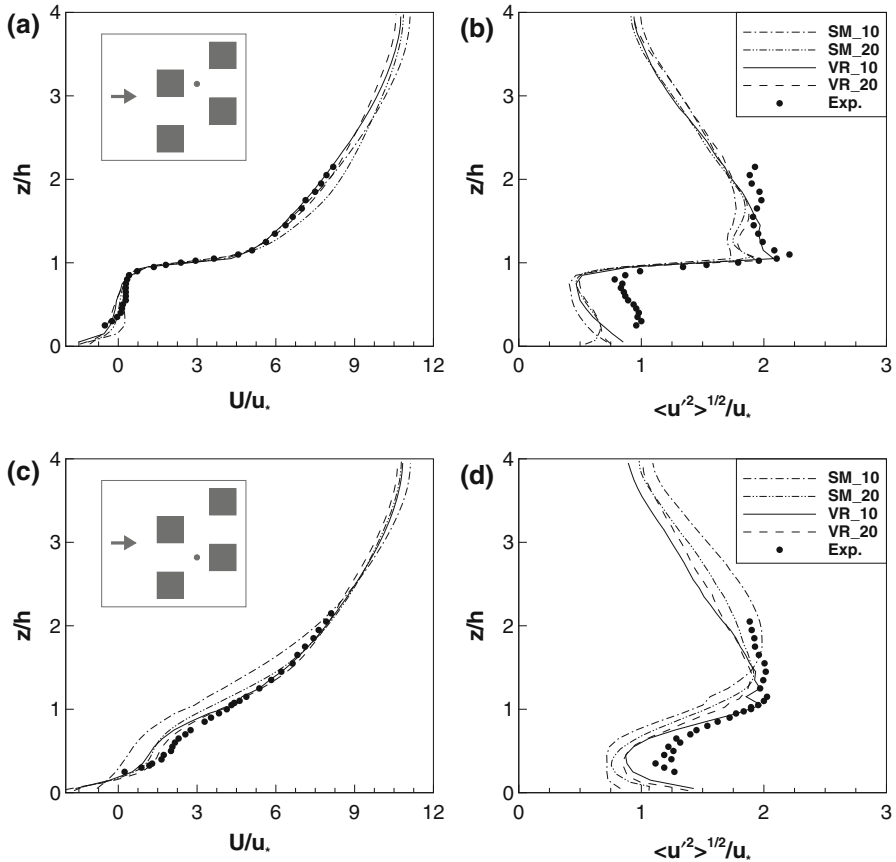


**Fig. 1** Model validation using the wind tunnel experiment [49]; vertical profiles of a mean streamwise velocity ( $U$ ) and **b** streamwise turbulence ( $\langle u'^2 \rangle^{1/2}$ ) normalized by the friction velocity ( $u_*$ ) behind of a cube; **c** mean streamwise velocity ( $U$ ) and **d** streamwise turbulence in front of a cube

were underestimated although both cases have captured the peak around the canopy height. Similar differences were reported by Xie and Castro[35].

### 2.3 Simulation settings

The simulation site in a complex urban street canyon is ‘Teheran Street’ of Seoul in Republic of Korea, which is one of the representative street canyons of Seoul where high-rise buildings are aligned along a wide road. Figure 2a shows the computational domain with a size of 900 m in the horizontal direction and 800 m in the vertical direction. The road in  $x$  or east-west direction surrounded by tall buildings is ‘Teheran Street’. The tallest building with a height of 135 m is noticeable at the intersection in the center of the domain. Figure 2b shows a side view of computational domain and the averaged building height (about 18.4 m).

In order to develop the turbulent flow over an urban canopy, a constant mean pressure gradient was applied. A periodic boundary condition was applied in the horizontal directions

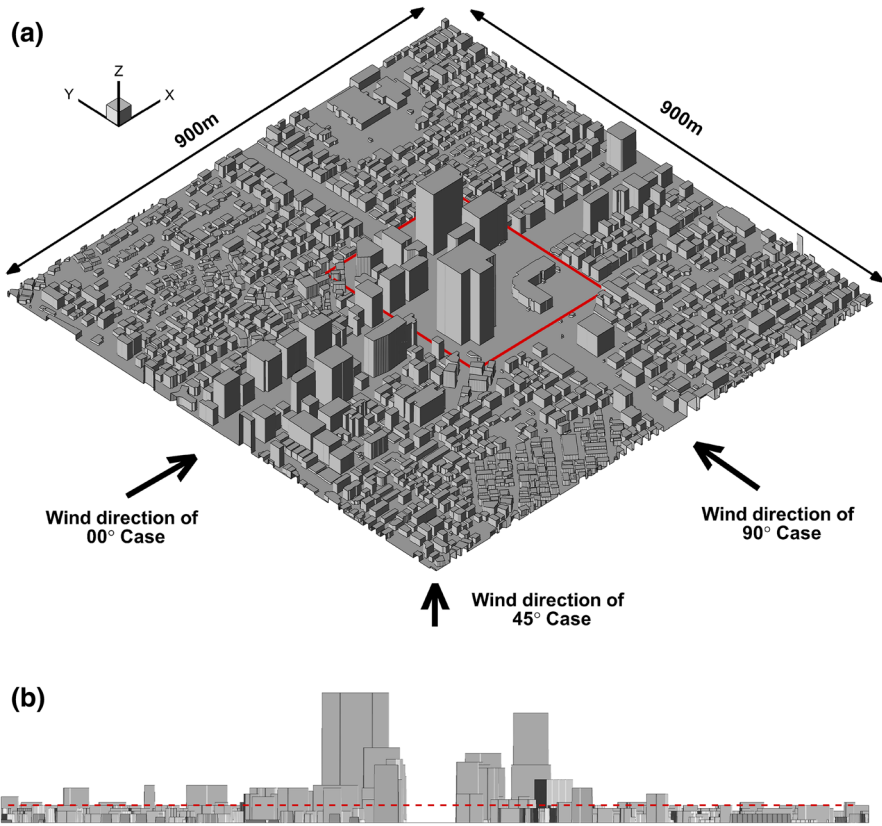


**Fig. 2** **a** Three-dimensional perspective view of the simulation domain (Teheran Street in Seoul, Republic of Korea) with three wind directions, as considered in our simulations. Note that a red box indicates a region in the vicinity of tall buildings. **b** Side view of the street canyon with the average height of skyline (red dotted line)

( $x$  and  $y$  directions) to avoid the situation in which uncertainty of the inlet flow condition contaminates the flow field. The horizontal domain size ( $900\text{ m} \times 900\text{ m}$ ) is large enough for the flow variables to be de-correlated, and the vertical domain size of  $800\text{ m}$  is high enough for the atmospheric boundary layer at a high altitude to be hardly affected by the buildings. For the species transport equation (3), however, a ventilation boundary condition was applied at the horizontal boundaries to prevent the species re-entering to the computational domain ( $\bar{Y}_\alpha = 0$ ). The geometry of the urban canopy at the bottom is mirrored to the top to maintain a statistical mirror condition at the channel mid-height instead of enforcing the slip condition there. The flow field in the top half region is also used to obtain more converged statistical data. At the solid surface, the no-slip condition was applied. A uniform mesh of 10.125 million cells with  $225 \times 225 \times 200$  grid points ( $4\text{ m} \times 4\text{ m} \times 4\text{ m}$  per cell) was used. Given that the length scale of the smallest buildings is on the order of  $10\text{ m}$ , a grid size of  $4\text{ m}$  might be not sufficient for full resolution. The choice of  $4\text{ m}$ , however, is the maximum within the capability of our computer resources. The time step ( $\delta t$ ) is adjusted so that the Courant–Friedrichs–Lewy (CFL) condition is satisfied: In each mesh cell of dimension  $\Delta x$  by  $\Delta y$  by  $\Delta z$  with velocity components  $u$ ,  $v$  and  $w$ , the CFL number defined by  $CFL =$

$\delta t \max(|u|/\Delta x, |v|/\Delta y, |w|/\Delta z)$  is maintained at 1. All statistics are averaged for at least 3,000 s after a transient run of 1,500 s.

Three flow directions are considered to investigate the SGS model performance, flow characteristics and dispersion characteristics: Wind blowing parallel to the street canyon (referred to as  $0^\circ$  case); wind blowing at a  $45^\circ$  inclined to the street canyon ( $45^\circ$  case); and wind blowing perpendicular to the street canyon ( $90^\circ$  case). Those are shown in Fig. 2. Flow direction is adjusted by the mean horizontal pressure gradient.

## 2.4 Grid sensitivity

Before proceeding further, we performed a grid dependency study for simulations of flow over the urban street canyon by using different grid resolutions in a reduced computational domain ( $600 \text{ m} \times 600 \text{ m} \times 800 \text{ m}$ ). Figure 3a–c show time-averaged velocity magnitudes at the height of 30 m for a uniform grid spacing with 4, 8 and 16 m, respectively. Overall trends of the predicted velocity fields are similar; however, for the finest grid resolutions higher

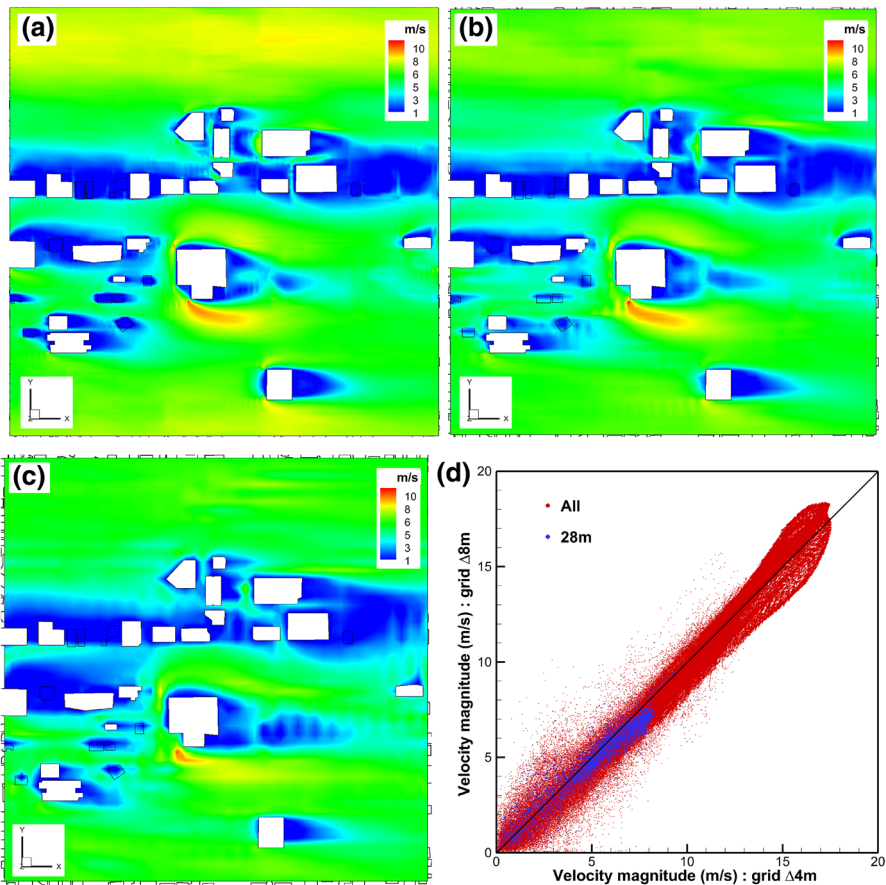


**Fig. 3** The effect of different grid resolutions ( $\Delta$ ) on the time-averaged velocity magnitude at the height of 30 m; **a**  $\Delta = 4$  m, **b**  $\Delta = 8$  m, and **c**  $\Delta = 12$  m. Scatter plot of the velocity magnitudes for grid resolutions with 4 and 8 m



velocity magnitudes are observed in built-up regions while the recirculating zone behind the tall building is slightly smaller. Figure 3d shows a scatter plot of velocity magnitudes for the grid spacings with 4 and 8 m. Red and blue dots represent the velocity magnitude on all grid points and grid points at the height of 30 m, respectively. The predicted velocity magnitudes show linear correlations for the entire computational domain. Larger deviations of velocity magnitudes are expected near the built-up regions at lower or higher height while the deviations at the height of 30 m are relatively small. The  $L_2$ -norm difference between velocity magnitudes for the grid spacing with 4 and 8 m is about 0.9 m/s while the difference is about 1.3 m/s between those for the grid spacings with 4 and 12 m. Although the grid test shows a weak convergence for the velocity magnitudes, the overall trends show that the grid spacing with 4 m may provide reasonable results for the flow and dispersion over urban street.

### 3 Subgrid scale model assessment

To investigate the performance of the SGS models, turbulent statistics, particularly various shear stresses, are compared for SM and VR. Raupach and Shaw [50] derived a spatially averaged formulation on a plant canopy flow. The filtered velocity component  $\bar{U}_i$  can then be decomposed into three components,

$$\bar{U}_i(x, y, z, t) = U_i(z) + \tilde{u}_i(x, y, z) + u'_i(x, y, z, t), \tag{25}$$

where  $U_i$  is the time and horizontal space averaged velocity,  $\tilde{u}_i$  is the spatial variation to  $U_i$ , and  $u'_i$  is the turbulent fluctuation. Averaging the filtered Navier-Stokes equation in time and space with the above decomposition produces various shear stress terms including the dispersive stress ( $\rho \langle \tilde{u}_i \tilde{u}_j \rangle$ ) [51]. Thus, the total shear stress is a sum of four stress components: Reynolds shear stress ( $\rho \langle u'_i u'_j \rangle$ ), dispersive stress ( $\rho \langle \tilde{u}_i \tilde{u}_j \rangle$ ), SGS stress ( $\rho \langle -\tau'_{ij} \rangle$ ), and viscous stress ( $\rho \nu \frac{\partial U_i}{\partial z}$ ), where the bracket denotes the horizontal space average, and directions 1 and 3 imply the mean wind and vertical directions, respectively.

Figures 4a–c show the averaged stress component profiles normalized by  $\rho u_*^2$  in the vertical direction for the cases of  $0^\circ$ ,  $45^\circ$  and  $90^\circ$ , respectively. In the legend, ‘SM\_TOT’ is the total stress obtained by SM and ‘VR\_SGS’ is the SGS stress component obtained by VR. The linear distribution of the total stress extrapolates to 1 at the bottom for all cases, confirming complete development. The maximum total stress is observed around the height of the tallest building, 135 m. As the wind direction changes, the shape of the total stress profile is different. In the  $0^\circ$  case, the tall buildings arrangement along the street canyon causes maximum peak to be sharp. For the  $0^\circ$  and  $45^\circ$  cases, the dispersive stress above the tallest building height shows negative values. As expected, the viscous stress is negligibly small even very near the surface. Among the stress components, the SGS stress, the contribution by the SGS model, is very small, while the Reynolds stress is dominant for all cases. However, the portion of the SGS stress in total stress is not negligible near the ground, which is the pedestrian level.

To identify the role of the SGS models in detail, the SGS stress normalized by  $\rho u_*^2$  in the vertical direction for the cases of  $0^\circ$ ,  $45^\circ$  and  $90^\circ$  with SM and VR is presented in Fig. 5a. For all wind directions, SM yields larger SGS stress than VR. The peaks occurred at several points including the tallest building height and the average building height, implying that the building edges are the source of the SGS stress. While maximum Reynolds stress occurs at the height of 135 m, SGS stress is maximum at the mean building height. Figure 5b shows

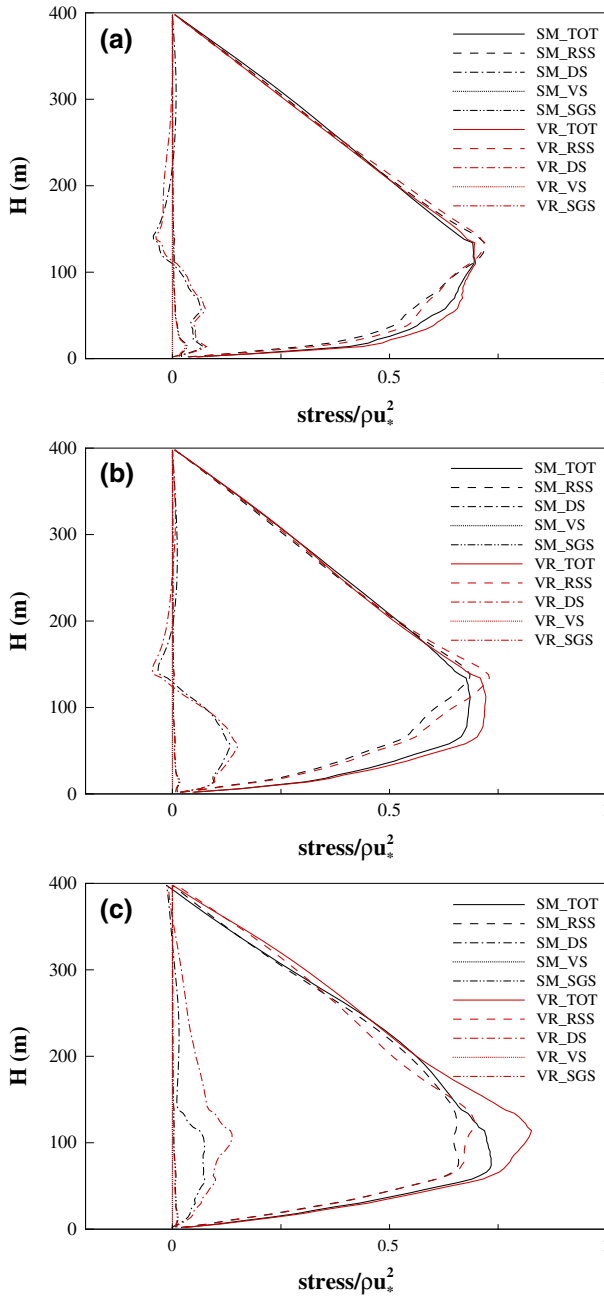


**Fig. 4** Averaged stress component profiles normalized by  $\rho u_*^2$  in the vertical direction; **a**  $0^\circ$  case; **b**  $45^\circ$  case; **c**  $90^\circ$  case. Note that TOT, RSS, DS, VS and SGS represent total stress, Reynolds shear stress, dispersive stress, viscous stress and SGS stress, respectively

the averaged eddy viscosity profiles in the vertical direction for the cases of  $0^\circ$ ,  $45^\circ$  and  $90^\circ$  with SM and VR. Eddy viscosity profile has a similar shape to the SGS stress profile. For all wind directions, SM produces larger eddy viscosity and SGS stress than VR.

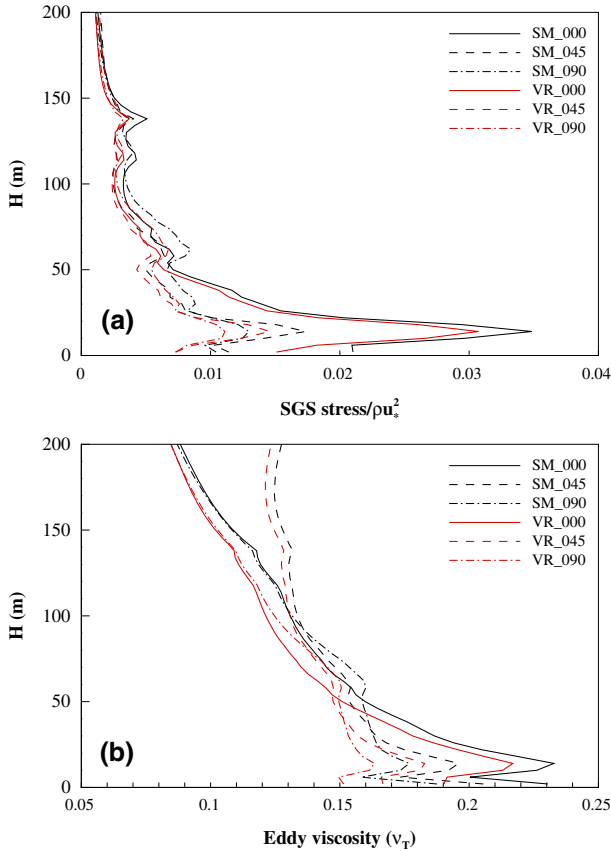


**Fig. 5** **a** Averaged SGS stress profiles normalized by  $\rho u_*^2$  in the **vertical** direction, **b** the averaged eddy viscosity profiles in the vertical direction for the case of  $0^\circ$ ,  $45^\circ$  and  $90^\circ$  with SM and VR

We investigate time averaged but local eddy viscosity in order to study local influences of the SGS models in detail. Figure 6a, b show eddy viscosity iso-surface ( $\nu_T = 0.25 \text{ m}^2/\text{s}$ ) for the case of  $0^\circ$  with SM and VR, respectively. Regardless of the SGS models, large values of eddy viscosity are mainly distributed near the surfaces and buildings, causing high turbulent motion. Consistent with the SGS stress of Fig. 5, the eddy viscosity of SM is more prevalent than that of VR for the given  $\nu_T$  level. Figure 6c shows correlations between time averaged eddy viscosities for the models at all grid points. The general trend of the scatter plot shows that SM estimates higher eddy viscosity than VR. Especially, a local eddy viscosity of SM is more than two times larger than that of VR at  $\nu_{T,VR} \approx 0.2 \text{ m}^2/\text{s}$ , while the difference of time and spatially averaged eddy viscosity between the two models is less than 7%, as also shown in Fig. 5b. Figure 6d shows local positions where the eddy viscosity of SM is 1.25 times larger than that of VR. Similar to the observation in Fig. 6a, b, it is evident that the eddy viscosity of SM is higher near building walls and street canyon surface than that of VR, but a difference of eddy viscosity between two models is not remarkable in the vortex regions of the buildings' leeward side. This is related to the fact that the Smagorinsky SGS model with a constant coefficient overestimates eddy viscosity near the blunt bodies. Given the dispersion near buildings heavily depends on turbulence there and that prediction of turbulence in LES

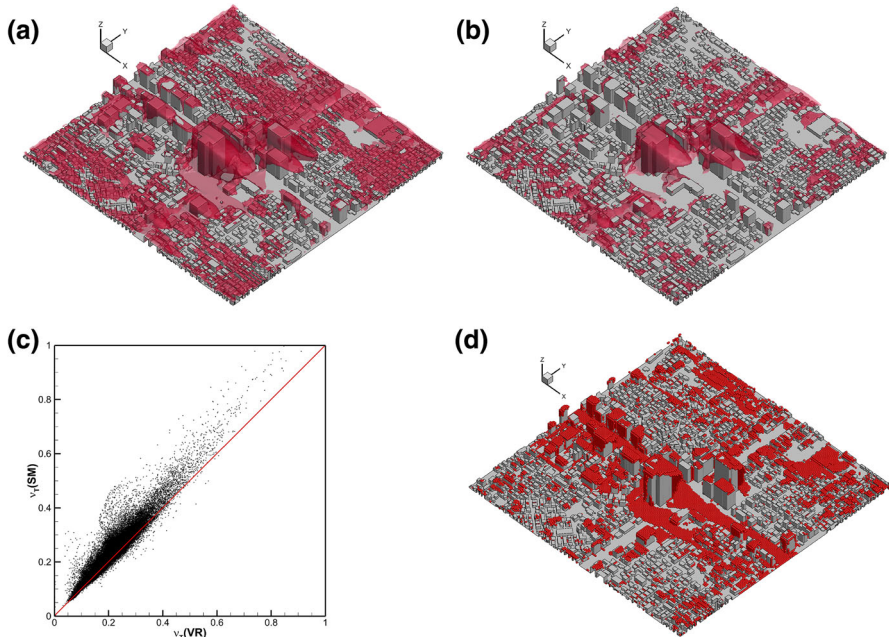


**Fig. 6** Time averaged eddy viscosity iso-surface ( $v_T = 0.25 \text{ m}^2/\text{s}$ ) for the case of  $0^\circ$  with **a** SM and **b** VR. Scatter plots of **c** correlations between time averaged eddy viscosities of SM and VR models at all grid points, and **d** local positions where the ratio of eddy viscosities ( $v_{T,SM}/v_{T,VR}$ ) is larger than 1.25

of urban flow is strongly associated with the small-scale SGS model, selection of the optimal SGS model is important.

Through the investigation of the SGS stress and eddy viscosity, we found that SM predicts larger modeled stress. In the simulation by SM, the sub-grid scale eddy viscosity does not vanish at the flow region where the SGS dissipation should theoretically be zero, e.g., near the wall and laminar flow region. On the other hand, VR guarantees that the SGS eddy viscosity vanishes for any part of flow where the SGS dissipation is expected to be zero. This property is important because the model coefficient does not have to vary significantly in space. Vreman [44] showed that the model with a fixed coefficient predicts accurate statistics for turbulent channel flow without introducing any wall damping function. This indicates that the model can be applied to flows in complex geometry which has no homogeneous direction. Thus, VR may be a good candidate for the eddy viscosity model to compensate the defect of SM for non-homogeneous flows.

#### 4 Flow characteristics

As discussed in the previous section, VR appears to be more proper for the simulation of flows in complex geometry such as an urban street canyon than SM. In this section, the flow characteristics in a complex urban street canyon are investigated using the Vreman SGS model for the cases of three wind directions,  $0^\circ$ ,  $45^\circ$  and  $90^\circ$ .

Figure 7 shows instantaneous wind distribution at the height of 2 m for the three wind directions. For all cases, there are weak winds in the built-up area, and strong winds are

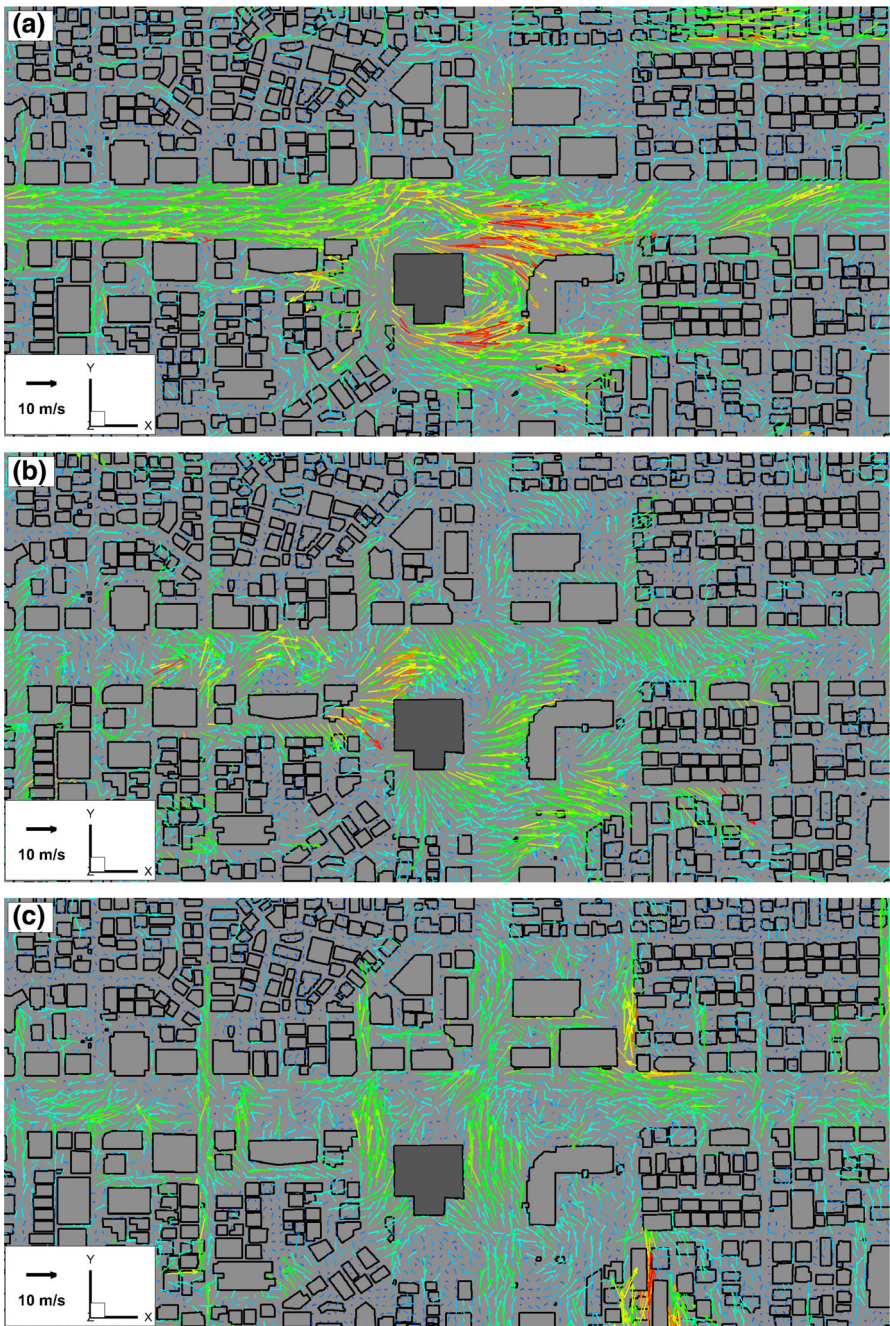


**Fig. 7** Instantaneous flow field vector distribution in the street canyon at the height of 2 m: **a**  $0^\circ$  case; **b**  $45^\circ$  case; **c**  $90^\circ$  case. The dark building in the center denotes the tallest building. The *vector color* denotes the magnitude of velocity

observed around the high-rise buildings. When the wind direction is parallel to the street canyon (case of  $0^\circ$ ), a high speed region is observed along the street canyon. For the case of  $45^\circ$ , jet-like flow patterns into the street canyon are observed, and the flow direction is rearranged, eventually following the canyon direction. For the cases of  $45^\circ$  and  $90^\circ$ , in the street canyon, there are local weak winds behind the buildings. Due to an entrainment of upper air downward, a reversed flow can be observed particularly in front of the tallest building (the dark building in the center). Commonly for all wind directions, a very strong wind is observed at both sides of the tallest building.

To investigate the flow pattern inside the street canyon, wind speed and turbulent kinetic energy (TKE) are averaged along the street canyon direction ( $x$ -direction) for each case. Hereafter, this averaging process is called the ‘depth-average’. Figure 8 shows contours of the depth-averaged mean velocity. For the case of  $0^\circ$  (Fig. 8a), wind speed contour shape resembles the sky-line of the urban street canyon. Mean velocity in the street canyon is larger than that in other regions. For the case of  $45^\circ$  (Fig. 8b), however, mean velocity gradually decreases in the canyon due to the formation of recirculating flows behind windward buildings. In this case, pollutants tend to stagnate in the street canyon. Also, in the  $90^\circ$  case (Fig. 8c), the wind speed in the street canyon is the weakest. The ventilation of pollutants is not easy once pollutants are trapped in the recirculation zones.

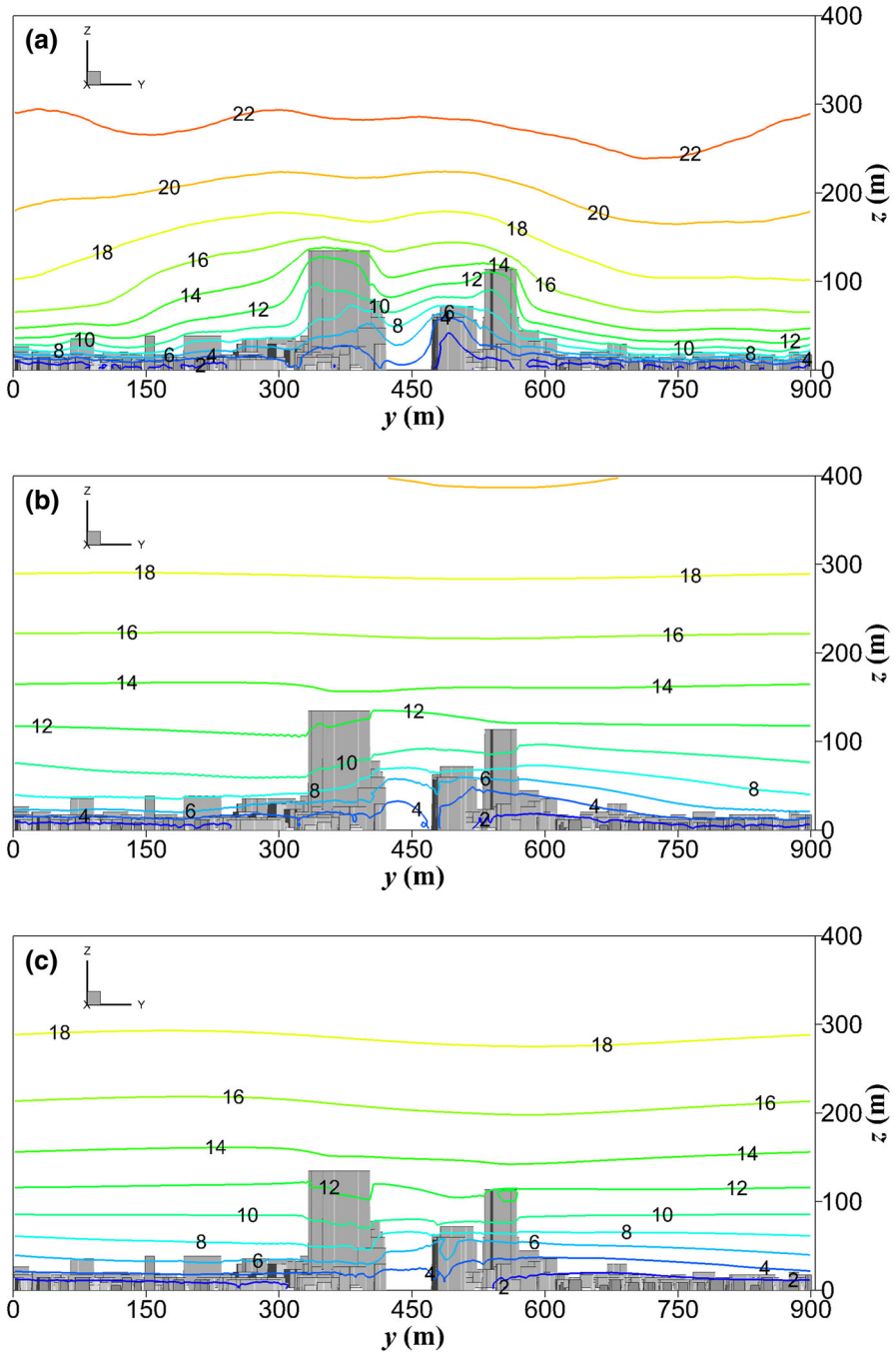
Figure 9 shows contours of the depth-averaged TKE. For the case of  $0^\circ$  (Fig. 9a), high level TKE occurs at the tops of tall buildings. This result is consistent with the Reynolds stress profile (see Fig. 4), which shows a peak in the same location. Contrary to the depth-averaged mean velocity contour (see Fig. 8a), the TKE level is lower in the street canyon than in other built-up areas. This implies that, if a wind blows along the street canyon, pollutants can advect more rapidly along the street canyon. For the cases of  $45^\circ$  (Fig. 9b) and  $90^\circ$  (Fig. 9c), TKE increases in the street canyon due to wake formation behind buildings. These phenomena will naturally affect the patterns of pollutant dispersion, which will be discussed in the next section.

Figure 10 shows three-dimensional stream tracers around tall buildings for the wind direction of  $0^\circ$ . Note that stream tracers are calculated by using the mean velocity field. The tracers turn around the tall building due to the high pressure in front of the building and then settle down to a pedestrian level. In a wake region, the helical motion of tracers is observed behind the tall building and the tracers eventually rise and form straight flow pattern due to the pressure recovery and uniformity of up-stream air. This dynamical flow pattern may suggest that the pollutant near the ground can be suspended near the top of the building.

To see the effect of tall buildings, we consider conditionally averaged flow statistics based on the region of interests which are categorized as ‘Tall building’ and ‘Built-up’. Here, ‘Tall building’ represents the region indicated by the red box in Figure 2 while the rest region of domain without ‘Tall building’ is named as ‘Built-up’. Three kinds of statistics such as mean wind speed, turbulent kinetic energy and Gust Equivalent Mean (GEM) wind speed [52] at the height of 10 m are listed in Table 1 for two regions. GEM wind speed ( $V_{GEM}$ ), a parameter for estimating pedestrian comforts, is defined as,

$$V_{GEM} = \max(V_M, V_G/1.85), \quad (26)$$

where  $V_M$  is the mean wind speed and  $V_G$  is the three seconds gust wind speed. Assuming Gaussian probability function of the wind speed,  $V_G$  can be obtained as  $V_G = V_M(1 + g_f I_u)$  where  $g_f$  and  $I_u$  are a peak factor and turbulence intensity, respectively, and typical value of  $g_f$  is 3.7. In general, mean wind speed and TKE for ‘Tall building’ are higher by the factor of 1.67 and 1.33 than for ‘Built-up’ region. The increasing factors slightly depends on the wind directions and are larger when the incoming wind is perpendicular to the main street canyon. It is worthy to note that GEM wind speed is almost two times higher than mean



**Fig. 8** Contour of the depth-averaged mean velocity (m/s) in the  $y - z$  plane: **a**  $0^\circ$  case; **b**  $45^\circ$  case; **c**  $90^\circ$  case

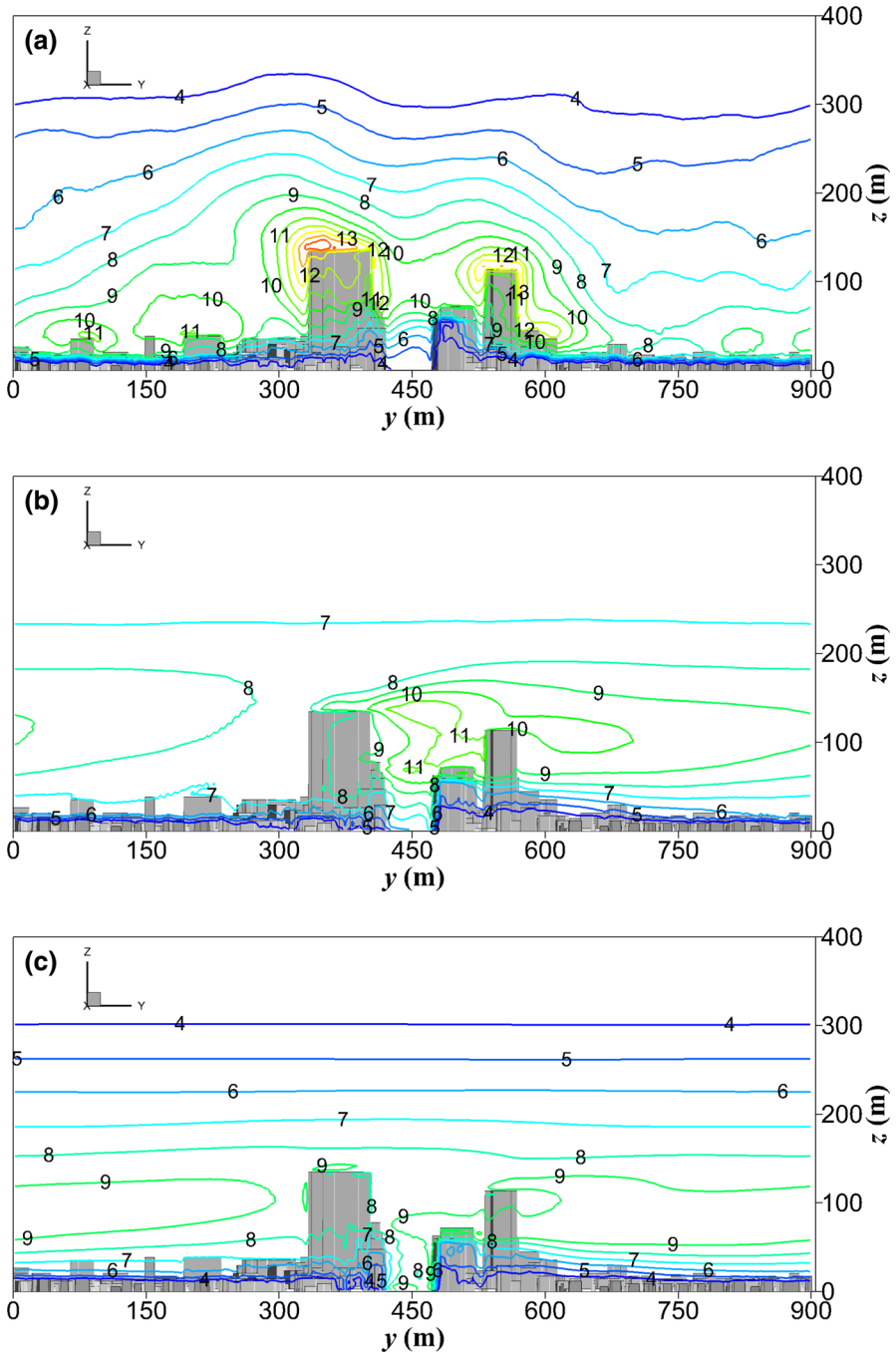


**Fig. 9** Contour of the depth-averaged TKE ( $\text{m}^2/\text{s}^2$ ) in the  $y - z$  plane: **a**  $0^\circ$  case; **b**  $45^\circ$  case; **c**  $90^\circ$  case





**Fig. 10** Streamlines passing around tall buildings for the wind direction of  $0^\circ$ : perspective views in **a** transverse and **b** streamwise directions; **c** top view; **d** side view

**Table 1** Wind statistics for tall building and built-up regions

Wind direction	Region	Mean speed (m/s)	TKE ( $\text{m}^2/\text{s}^2$ )	GEM (m/s)
0°	Tall building	4.43	2.98	8.11
	Built-up	3.06	2.39	5.93
45°	Tall building	4.14	2.97	7.74
	Built-up	2.41	2.33	5.06
90°	Tall building	3.33	3.11	6.86
	Built-up	1.80	2.10	4.03

wind speed, regardless of the wind directions. Also GEM wind speed for ‘Tall building’ is higher by the factor of 1.63 than for ‘Built-up’. This indicates that pedestrians will experience very uncomfortable gust or continuous high speed wind when they are walking around tall buildings.

Although it is not straightforward to generalize the characteristics of flow over a complex urban area, the presence of tall buildings plays an important role in defining the flow field within the urban canyon and intersection. Furthermore, obviously there exists a close relation among the flow near high-rise buildings, the flow direction, and the arrangement of buildings.

## 5 Dispersion characteristics

In order to investigate the dispersion characteristics in a complex urban area, a passive pollutant emission is simulated using LES combined with the mass transport equation. Air is selected as the gaseous pollutant to exclude the buoyancy effect. For identifying how the source location and wind direction influence dispersion pattern, two emission locations and three wind directions are considered. Simulation cases are listed in Table 2. One emission source is placed in the middle of the street canyon, represented as a black circle in Fig. 11. The other source is located in the built-up region, represented as a black circle in Figs. 12 and 13. Pollutants are emitted at a constant flow rate of 1.93 kg/s, and the corresponding vertical velocity is 0.1 m/s at the ground surface element of  $4\text{ m} \times 4\text{ m}$ . We also apply the industrial source complex (ISC3) model [53] based on a Gaussian plume model for the pollutant dispersion. Time-averaged wind speed field at the height of 2 m from the LES simulations is used for ISC3 model, assuming a neutral atmospheric condition.

Figures 11, 12, 13 show time-averaged mass fraction contours of pollutants at the height of 2 m for the cases of wind directions 0°, 45° and 90°, respectively. Concentration unit is a dimensionless mass fraction of the pollutant to air pollutant mixture. Color bands of the concentration level are exponentially expressed from  $10^{-5}$  to  $10^{-3}$ , and only concentration levels above  $10^{-5}$  are shown. In the case of wind direction 0°, most pollutants released from the street canyon disperse mostly within the street canyon as shown in Fig. 11a. Flows induced by the canyon make pollutants advect within the canyon, thus producing a moderately high

**Table 2** Dispersion simulation cases

Case	Source position	Wind direction
SC00	Street canyon	0°
BR45	Built-up region	45°
BR90	Built-up region	90°

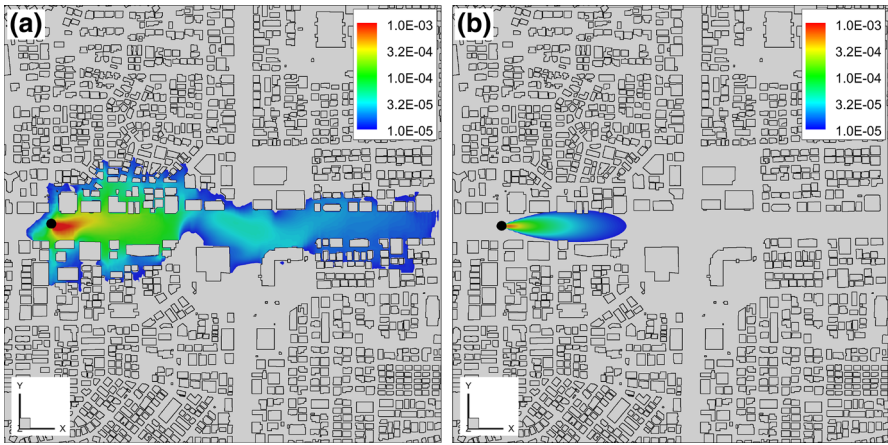


**Fig. 11** Contours of averaged-mass fraction of pollutants at the height of 2 m for the case SC00; **a** FDS and **b** ISC3

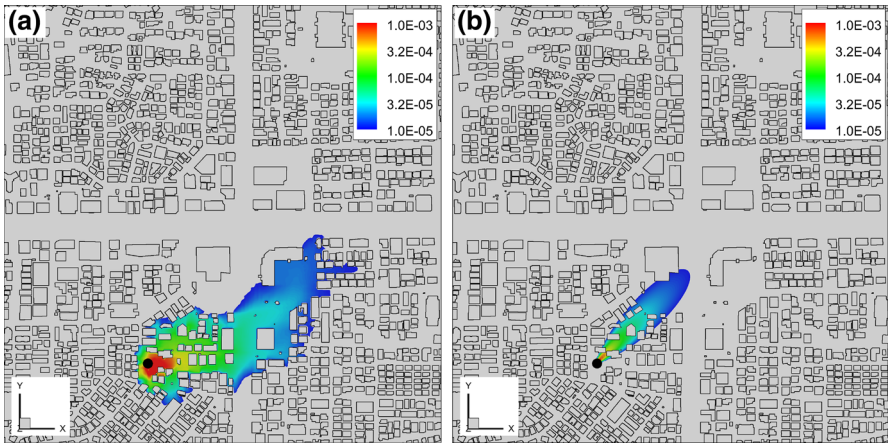


**Fig. 12** Contours of averaged-mass fraction of pollutants at the height of 2 m for the case BR45; **a** FDS and **b** ISC3

concentration level inside the canyon. This dispersion pattern is obviously different from that of a Gaussian plume resulting from ISC3 model (Fig. 11b). Pollutants in the LES simulation are drifted much further downstream due to accelerated wind fields near the tall building shown in Fig. 7a.

When a wind blows 45° obliquely with the street canyon, for the emission source located in the built-up region (BR45 case) in Fig. 12a, pollutants spread immediately near the source location due to high turbulence level and narrow passages in between the buildings. Coming out of the built-up area, pollutants are angled by 45°. It is interesting to note that, although the tallest building near the intersection is in the expected path of the plume, the plume cannot penetrate into the area near the building due to the recirculating flow pattern there. Also, pollutants spread the right-lower block crossing the street and are expected to be accumulated near the L-shape building while ISC3 model predicts the pollutants remained at the same concentration level in the block where the emission source is located, as shown in Fig. 12b.

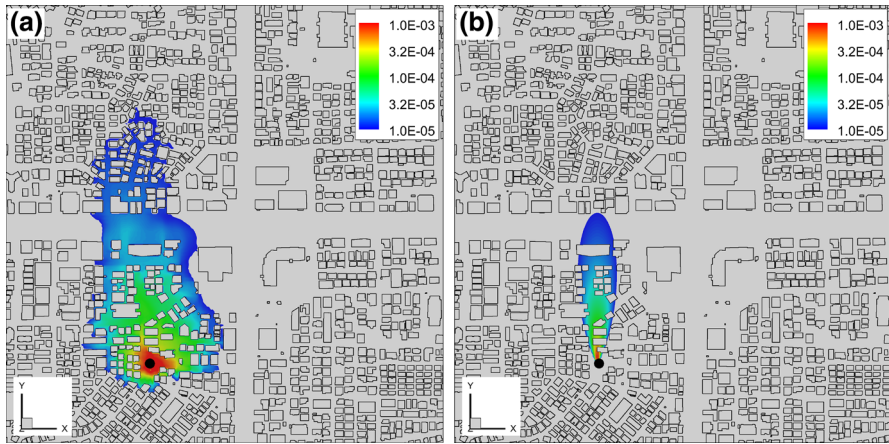


**Fig. 13** Contours of averaged-mass fraction of pollutants at the height of 2 m for the case BR90; **a** FDS and **b** ISC3

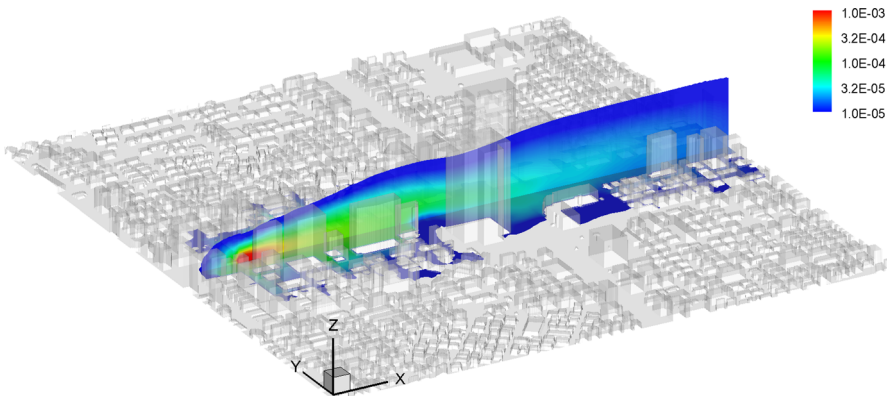


**Fig. 14** Three-dimensional perspective view of averaged mass fraction contours of pollutants for the case of wind direction  $0^\circ$  and emission source in the street canyon. *Vertical plane* is an  $x - z$  plane parallel to the street canyon passing through the emission source position. *Horizontal plane* is an  $x - y$  plane at the height of 2 m

When the emission source is in the built-up region, pollutants spread very widely near the source location due to recirculation flow between buildings. There are distinguished patterns in the street canyon, as shown in Fig. 13a. As pollutants are blocked and trapped between tall buildings, even a very low concentration level of  $10^{-6}$  is not found near the ground level. This indicates that pollutants are elevated due to the presence of blockages. Figure 13 also shows that pollutants in the LES simulation more widely spread in the left-upper block crossing the street canyon compared to pollutant dispersion in ISC3 model. In general, a simple Gaussian plume model under-estimates the pollutant dispersion boundaries (or ranges) compared to the LES results. A proper parametrization of building elevations, geometrical surface configuration or local turbulence effect is needed in Gaussian plume models for better predictions of pollutant dispersion.

Figure 14 shows a three-dimensional perspective view of time-averaged mass fraction contours of pollutants for the case of wind direction  $0^\circ$  with an emission source in the street

canyon. To examine the internal structure of the plume, mass fraction distributions at two sections are plotted. The *vertical plane* is an  $x - z$  plane parallel to the street canyon passing through the emission source position. The *horizontal plane* is an  $x - y$  plane at the height of 2 m. The plume center arises continuously toward the tallest building. As the recirculating flow in front of the tallest building and strong wakes behind the same building enhance the mixing of pollutants, the concentration level around the building is homogenized in a wide area.

## 6 Conclusions

Turbulent flow and dispersion characteristics over a complex urban street canyon in Seoul, Republic of Korea are investigated by LES. Two kinds of SGS models, the constant coefficient Smagorinsky model and the Vreman model, were tested to evaluate SGS model performance. For the two SGS models, the SGS stress among the stress components is small on average but the portion of the SGS stress in total stress is not negligible near the surface or the edge of buildings. Our comparison of subgrid scale model performance in a complex urban geometry shows that the Vreman model is a good candidate for a proper eddy viscosity model. In our investigation of SGS stress and eddy viscosity, the Vreman model indeed compensated for the defect of the constant-coefficient Smagorinsky model for non-homogeneous flows such as a flow passing through an urban area.

Through simulations of flow over a complex urban area, we found that there exist some patterns of flow in the street canyon due to flow distortion induced by high-rise buildings alongside the street canyon. When winds blow parallel to the street canyon, the mean velocity in the street canyon is maintained at a moderate level. When winds blow obliquely with or perpendicular to the street canyon, however, jet-like flows are found between tall buildings arranged along the street canyon. The tallest building at an intersection also significantly alters wind distribution in the street canyon by generating the recirculating flow in the windward region and the wake flow in the leeward region. On the other hand, turbulence kinetic energy contours show a different pattern from the mean velocity distribution in the street canyon. Turbulence is very active near the tops of buildings when winds blow parallel to the street canyon, while strong turbulence is found in the street canyon when winds blow obliquely or perpendicular to the street canyon. For the Gust Equivalent Mean wind speed that indicates the pedestrian comfort, the GEM wind speed is almost two times higher than mean wind speed, regardless of the wind directions. Moreover, higher GEM wind speed is expected near the tall building region compared to the speed in the built-up region.

The dispersion characteristics of ISC3 model that is based on the assumption of the pollutants dispersion with Gaussian distribution cannot represent local variations affected by specific geometries like buildings. On the other hand, an investigation of dispersion characteristics based on the present LES showed that distinguished patterns are observed depending on pollutant emission location and wind direction. When an emission source is located in the built-up region, high turbulence level and direct influence of compactly distributed buildings cause pollutants to spread widely near the source location. On the other hand, when an emission source is located in the street canyon, pollutants disperse mainly within the street canyon, and high concentration pollutants propagate rapidly when wind direction is parallel with the street canyon orientation. Pollutants tend to advect within the canyon maintaining a moderately high concentration level when wind direction is inclined or perpendicular to the street canyon. Tall buildings play an important role in determining dispersion pattern by forming recirculating flows around the buildings.

In our study, we did not consider the effect of turbulence generated by automobiles passing through the street canyon or trees on the street, which might be not negligible in complex practice. Thermal stratification and the convection effect were also not taken into account. These effects should be considered in future study of urban dispersion.

**Acknowledgments** This work was supported by the National Research Foundation of Korea(NRF) grant funded by the Korea government (R31-2008-000-10049-0, 20090093134, EDISON project: 2011-0029561) and Agency for Defense Development.

## References

1. Roth M (2000) Review of atmospheric turbulence over cities. *Q J R Meteorol Soc* 126(564):941–990
2. Hanna S, Britter R (2002) *Wind flow and vapor cloud dispersion at industrial and urban sites*. Wiley, New York
3. Batchvarova E, Gryning SE (2005) Progress in urban dispersion studies. *Theor Appl Climatol* 84:57–67
4. Collier CG (2006) The impact of urban areas on weather. *Q J R Meteorol Soc* 132:1–25
5. Souch C, Grimmond S (2006) Applied climatology: urban climate. *Prog Phys Geogr* 30:270–279
6. Fernando H, Lee S, Anderson J, Princevac M, Pardyjak E, Grossman-Clarke S (2001) Urban fluid mechanics: air circulation and contaminant dispersion in cities. *Environ Fluid Mech* 1:107–164
7. Cimarelli A, Perry S, Venkatram A, Weil J (1998) AERMOD: description of model formulation. US EPA
8. Scire J, Strimaitis D, Yamartino R (2000) A user's guide for the CALPUFF dispersion model. Earth Tech, Concord
9. Kim BG, Lee C, Joo S, Ryu KC, Kim S, You D, Shim WS (2011) Estimation of roughness parameters within sparse urban-like obstacle arrays. *Bound-Layer Meteorol* 139(3):457–485
10. Britter RE, Hanna SR (2003) Flow and dispersion in urban areas. *Ann Rev Fluid Mech* 35:469–496
11. Dobre A, Arnold S, Smalley R, Boddy J, Barlow J, Tomlin A, Belcher S (2005) Flow field measurements in the proximity of an urban intersection in London, UK. *Atmos Environ* 39:4647–4657
12. Balogun Aa, Tomlin AS, Wood CR, Barlow JF, Belcher SE, Smalley RJ, Lingard JJJ, Arnold SJ, Dobre A, Robins AG, Martin D, Shallcross DE (2010) In-street wind direction variability in the vicinity of a busy intersection in central London. *Bound-Layer Meteorol* 136(3):489–513
13. Inagaki A, Kanda M (2008) Turbulent flow similarity over an array of cubes in near-neutrally stratified atmospheric flow. *J Fluid Mech* 615:101–120
14. Kastner-Klein P, Plate E (1999) Wind-tunnel study of concentration fields in street canyons. *Atmos Environ* 33:3973–3979
15. Khan IM, Simons RR, Grass AJ (2005) Upstream turbulence effect on pollution dispersion. *Environ Fluid Mech* 5:393–413
16. Tsang C, Kwok K, Hitchcock P (2012) Wind tunnel study of pedestrian level wind environment around tall buildings: effects of building dimensions, separation and podium. *Build Environ* 49:167–181
17. Pearce W, Baker C (1999) Wind tunnel tests on the dispersion of vehicular pollutants in an urban area. *J Wind Eng Ind Aerodyn* 80:327–349
18. Carpentieri M, Robins AG, Baldi S (2009) Three-dimensional mapping of air flow at an urban canyon intersection. *Bound-Layer Meteorol* 133:277–296
19. Li XX, Liu CH, Leung DY, Lam K (2006) Recent progress in CFD modeling of wind field and pollutant transport in street canyons. *Atmos Environ* 40:5640–5658
20. Assimakopoulos V (2003) A numerical study of atmospheric pollutant dispersion in different two-dimensional street canyon configurations. *Atmos Environ* 37:4037–4049
21. Baik JJ, Kang YS, Kim JJ (2007) Modeling reactive pollutant dispersion in an urban street canyon. *Atmos Environ* 41:934–949
22. Huang Y, Hu X, Zeng N (2009) Impact of wedge-shaped roofs on airflow and pollutant dispersion inside urban street canyons. *Build Environ* 44:2335–2347
23. Lateb M, Masson C, Stathopoulos T, Bedard C (2010) Numerical simulation of pollutant dispersion around a building complex. *Build Environ* 45:1788–1798
24. Hang J, Li Y, Sandberg M, Buccolieri R, Sabatino SD (2012) The influence of building height variability on pollutant dispersion and pedestrian ventilation in idealized high-rise urban areas. *Build Environ* 56:346–360
25. Wang X, McNamara K (2006) Evaluation of CFD simulation using RANS turbulence models for building effects on pollutant dispersion. *Environ Fluid Mech* 6:181–202

26. Gartmann A, Muller M, Parlow E, Vogt R (2012) Evaluation of numerical simulations of  $C O_2$  transport in a city block with field measurements. *Environ Fluid Mech* 12:185–200
27. Koutsourakis N, Bartzis J, Markatos N (2012) Evaluation of reynolds stress,  $k - \epsilon$  and RNG  $k - \epsilon$  turbulence models in street canyon flows using various experimental datasets. *Environ Fluid Mech* 12:379–403
28. Gousseau P, Blocken B, Stathopoulos T, van Heijst G (2011) CFD simulation of near-field pollutant dispersion on a high-resolution grid: a case study by LES and RANS for a building group in downtown Montreal. *Atmos Environ* 45(2):428–438
29. Tominaga Y, Stathopoulos T (2010) Numerical simulation of dispersion around an isolated cubic building: model evaluation of RANS and LES. *Build Environ* 45:2231–2239
30. Tominaga Y, Stathopoulos T (2011) CFD modeling of pollution dispersion in a street canyon: comparison between LES and RANS. *J Wind Eng Ind Aerodyn* 99(4):340–348
31. Salim SM, Cheah SC, Chan A (2011) Numerical simulation of dispersion in urban street canyons with avenue-like tree plantings: comparison between RANS and LES. *Build Environ* 46:1735–1746
32. Hanna S, Tehrani S, Carissimo B, Macdonald R, Lohner R (2002) Comparisons of model simulations with observations of mean flow and turbulence within simple obstacle arrays. *Atmos Environ* 36:5067–5079
33. Baker J, Walker HL, Cai X (2004) A study of the dispersion and transport of reactive pollutants in and above street canyons—a large eddy simulation. *Atmos Environ* 38:6883–6892
34. Kanda M, Moriwaki R, Kasamatsu F (2004) Large-eddy simulation of turbulent organized structures within and above explicitly resolved cube arrays. *Bound-Layer Meteorol* 112(2):343–368
35. Xie Z, Castro IP (2006) LES and RANS for turbulent flow over arrays of wall-mounted obstacles. *Flow Turbul Combust* 76:291–312
36. Letzel MO, Krane M, Raasch S (2008) High resolution urban large-eddy simulation studies from street canyon to neighborhood scale. *Atmos Environ* 42:8770–8784
37. Li XX, Liu CH, Leung DY (2009) Numerical investigation of pollutant transport characteristics inside deep urban street canyons. *Atmos Environ* 43:2410–2418
38. Gu ZL, Zhang YW, Cheng Y, Lee SC (2011) Effect of uneven building layout on air flow and pollutant dispersion in non-uniform street canyons. *Build Environ* 46:2657–2665
39. Coceal O, Thomas T, Castro I, Belcher S (2006) Mean flow and turbulence statistics over groups of urban-like cubical obstacles. *Bound-Layer Meteorol* 121:491–519
40. Hanna SR, Brown MJ, Camelli FE, Chan ST, Coirier WJ, Kim S, Hansen OR, Huber AH, Reynolds RM (2006) Detailed simulations of atmospheric flow and dispersion in downtown Manhattan: an application of five computational fluid dynamics models. *Bull Am Meteorol Soc* 87:1713–1726
41. Patnaik G, Boris JP, Young TR, Grinstein FF (2007) Large scale urban contaminant transport simulations with miles. *J Fluids Eng* 129(12):1524–1532
42. Liu Y, Cui G, Wang Z, Zhang Z (2011) Large eddy simulation of wind field and pollutant dispersion in downtown Macao. *Atmos Environ* 45(17):2849–2859
43. Smagorinsky J (1963) General circulation experiments with the primitive equations. *Mon Weather Rev* 91(3):99–164
44. Vreman AW (2004) An eddy-viscosity subgrid-scale model for turbulent shear flow: algebraic theory and applications. *Phys Fluids* 16:3670–3681
45. McGrattan K, Hostikka S, Floyd J, Baum H, Rehm R, Mell W, McDermott R (2010) *Fire Dynamics Simulator (Version 5) Technical reference guide, vol 1: Mathematical model*. NIST
46. Germano M, Piomelli U, Moin P, Cabot WH (1991) A dynamic subgrid-scale eddy viscosity model. *Phys Fluids A* 3:1760–1765
47. Shah KB (1998) Large eddy simulations of flow past a cubic obstacle. Ph.D. thesis, Stanford University, Stanford
48. Werner H, Wengle H (1991) Large-eddy simulation of turbulent flow over and around a cube in a plate channel. In 8th Symposium on Turbulent Shear Flows. Technische University Munich, Munich, pp 155–168
49. Castro IP, Cheng H, Reynolds R (2006) Turbulence over urban-type roughness: deductions from wind-tunnel measurements. *Bound-Layer Meteorol* 118:109–131
50. Raupach MR, Shaw RH (1982) Averaging procedures for flow within vegetation canopies. *Bound-Layer Meteorol* 22:79–90
51. Finnigan J (2000) Turbulence in plant canopies. *Ann Rev Fluid Mech* 32:519–571
52. Lawson T (1990) The determination of the wind environment of a building complex before construction. University of Bristol, Report number 9025
53. EPA (1995) User's guide for the industrial source complex (ISC3) dispersion models. Report number EPA-454/B-95-003b, US Environmental Protection Agency